

Analysis of gravity waves structures visible in noctilucent cloud images

P.-D. Pautet ^{a,*}, J. Stegman ^b, C.M. Wrasse ^c, K. Nielsen ^d, H. Takahashi ^e, M.J. Taylor ^a, K.W. Hoppel ^f, S.D. Eckermann ^f

^a Center for Atmospheric and Space Sciences, Utah State University, Logan, UT, USA

^b Department of Meteorology, Stockholm University, Stockholm, Sweden

^c Instituto de Pesquisa e Desenvolvimento, Universidade do Vale do Paraíba, São José dos Campos SP, Brazil

^d Computational Physics Inc., Boulder, CO, USA

^e Instituto Nacionais de Pesquisas Espaciais, São José dos Campos SP, Brazil

^f Naval Research Laboratory, Washington, DC, USA

*Corresponding author. Tel.: +1 4357978128.

E-mail address: dominiquepautet@gmail.com

Keywords:

Noctilucent clouds (NLC); Mesosphere lower thermosphere (MLT); Gravity waves; Image processing

Report Documentation Page				Form Approved OMB No. 0704-0188	
Public reporting burden for the collection of information is estimated to average 1 hour per response, including the time for reviewing instructions, searching existing data sources, gathering and maintaining the data needed, and completing and reviewing the collection of information. Send comments regarding this burden estimate or any other aspect of this collection of information, including suggestions for reducing this burden, to Washington Headquarters Services, Directorate for Information Operations and Reports, 1215 Jefferson Davis Highway, Suite 1204, Arlington VA 22202-4302. Respondents should be aware that notwithstanding any other provision of law, no person shall be subject to a penalty for failing to comply with a collection of information if it does not display a currently valid OMB control number.					
1. REPORT DATE 2010		2. REPORT TYPE		3. DATES COVERED 00-00-2010 to 00-00-2010	
4. TITLE AND SUBTITLE Analysis of gravity waves structures visible in noctilucent cloud images				5a. CONTRACT NUMBER	
				5b. GRANT NUMBER	
				5c. PROGRAM ELEMENT NUMBER	
6. AUTHOR(S)				5d. PROJECT NUMBER	
				5e. TASK NUMBER	
				5f. WORK UNIT NUMBER	
7. PERFORMING ORGANIZATION NAME(S) AND ADDRESS(ES) Center for Atmospheric and Space Sciences,Utah State University,Logan,UT				8. PERFORMING ORGANIZATION REPORT NUMBER	
9. SPONSORING/MONITORING AGENCY NAME(S) AND ADDRESS(ES)				10. SPONSOR/MONITOR'S ACRONYM(S)	
				11. SPONSOR/MONITOR'S REPORT NUMBER(S)	
12. DISTRIBUTION/AVAILABILITY STATEMENT Approved for public release; distribution unlimited					
13. SUPPLEMENTARY NOTES					
14. ABSTRACT					
15. SUBJECT TERMS					
16. SECURITY CLASSIFICATION OF:			17. LIMITATION OF ABSTRACT Same as Report (SAR)	18. NUMBER OF PAGES 35	19a. NAME OF RESPONSIBLE PERSON
a. REPORT unclassified	b. ABSTRACT unclassified	c. THIS PAGE unclassified			

Abstract

The noctilucent clouds (NLC) are high-altitude bright cloud formations visible under certain conditions from high-latitude places during the summer months. Even if the exact nature of these clouds still remains a mystery, they are an efficient tracer of the dynamic processes at their level, particularly the gravity waves propagating from the stratosphere through the mesopause layer. In this paper, we describe a technique developed to analyze the structures visible in the NLC images taken every summer night since 2004 from Stockholm, Sweden (59.4°N). The parameters of 30 short-period gravity wave events have been measured and compared with older datasets obtained mostly from low and mid-latitude sites, using airglow imaging techniques. The horizontal wavelengths are in good agreement with previous results while the observed horizontal phase speeds exhibit smaller values than for other sites. The directionality of the waves presents strong poleward preference, traditionally observed during the summer season. This anisotropy and the difference in the phase speed distribution cannot be explained by the filtering due to the background wind field but more probably by the position of the gravity waves sources, located to the south of the observation site.

1. Introduction

Noctilucent clouds (NLCs) are thought to be composed of small ice particles but their process of formation is still a hot research topic. They occur in the upper mesosphere, between 80 and 85 km, with a mean altitude of 82.9 km (Gadsden and Schröder, 1989), and are most frequently observed from the ground between 50 and 65° of latitude. Their appearance is very similar to cirrostratus clouds, which are also composed of ice but develop in the troposphere; however their color is generally silvery blue (Fig. 1). Each

NLC may be composed of different forms, classified in four major: veil (Type I), bands (Type II), billows or waves (Type III) and whirls (Type IV). These four major types are then separated in several subdivisions (Gadsden and Parviainen, 1995). NLCs were first reported in 1884 (Leslie, 1884; Jesse, 1889), but their occurrence and brightness are claimed to be increasing, especially during the last 30 years (Gadsden, 2002; Klostermeyer, 2002; Deland et al., 2003]. Furthermore, sightings from unusual mid-latitude sites have more often been reported (Taylor et al., 2002; Wickwar et al., 2002; Nielsen et al., this issue). Following these observations, it has been suggested that the occurrence of NLCs may be a very sensitive indicator of the changes in the atmosphere composition and dynamics, and possibly of the Earth global change.

Besides the study of their own properties (Witt, 1962; Fogle and Haurwitz, 1966), NLCs are also an interesting tool for analyzing the dynamics of the upper atmosphere. In fact, they work as a tracer of the coherent structures forming or propagating at their level (e.g., Fritts et al., 1993; Chandran et al., 2009). Optical studies of similar phenomena have already been done using the mesopause region airglow emissions as markers of the waves (e.g., Taylor et al., 1997; Pautet et al., 2005; Nielsen et al., 2009). Since the NLC layer is significantly thinner than a typical airglow layer (2-3 km compared to 8-9 km) (She and Lowe, 1998), the observed wave signatures should appear much more clearly in NLC images and thus could be studied in much better detail. Also, the airglow imaging technique requires conditions that are not always encountered at high-latitudes because of the persistent twilight in the summer months and the possible auroral contamination of these faint emissions throughout the year. Hence, imaging NLCs provide a method to perform summer-time observations, and in conjunction with airglow observations, complete a full seasonal study of wave structures.

73 Several types of structures, with different origins, may be analyzed using the patterns
74 visible in the NLC images (Haurwitz, 1961), like the short-period ($<1\text{h}$) gravity waves (or
75 bands) and the ripples (or billows). The background wind might also be determined
76 (Fogle and Haurwitz, 1966, Fritts et al., 1993).

77 The small-scale waves, termed ripples or billows, are short-lived (typically few tens
78 of minutes) structures due to localized regions of convective or shear instabilities,
79 generated in-situ at mesospheric altitudes (Taylor and Hapgood, 1990; Fritts et al., 1993;
80 Fritts et al., 1994). They may also be the result of the breaking of a freely propagating
81 gravity wave (Horinouchi et al., 2002).

82 Gravity waves are the oscillations of air parcels by the lifting force of buoyancy and
83 the restoring force of gravity (Hines, 1960). They can be generated by several sources: in
84 the troposphere by thunderstorm updrafts, frontal systems or airflow over mountains, but
85 also by interaction with the polar jet stream, geostrophic adjustments, wave-wave
86 interactions or wave breaking. These waves propagate vertically and horizontally and
87 may be observed during several hours. Their horizontal wavelength may vary from 10 to
88 more than 100 kilometers. They play an essential role in affecting the dynamics and
89 structures of the middle and upper atmosphere and participate in driving the thermal
90 structure and setting up large-scale meridional circulation in the mesosphere and lower
91 thermosphere (MLT) region (altitude $\sim 60\text{--}100\text{ km}$). Freely propagating gravity waves
92 actively transport energy and momentum from the troposphere into the MLT region,
93 where they deposit their energy and transfer their momentum to the mean flow when
94 breaking in the more rarefied air (Lindzen, 1981; Fritts and Alexander, 2003). They also
95 have direct effects on the noctilucent clouds: horizontal variations in cloud particle
96 concentration, decrease of ice crystal size and average cloud albedo for short-period (less

97 than a few hours) gravity waves, inhibition of the NLC formation due to temperature
98 perturbations (Jensen and Thomas, 1994; Rapp et al., 2002).

99 When seen from the ground, all these waves are distorted by the geometry of the
100 observation. The spherical shape of the atmospheric layer where NLCs reside and the
101 refraction due to propagation through the atmospheric medium, modify the shape, the
102 size and the observed speed of the waves. All these parameters are necessary to
103 understand the gravity waves properties, thus, it is important to work with
104 geographically-oriented, linear-scaled images to permit the accurate measurement of
105 these values.

106 In this paper, we will describe a technique developed to analyze short-period gravity
107 wave structures observed in NLC images. Following a detailed description of the
108 problem geometry, the original images will be projected onto a linear geographic grid in
109 a process known as “unwarping”. These new images will be similar to satellite-type
110 pictures: the NLC layer as seen from the top, looking downward, oriented due to the
111 geographic north, and represented with a linear scale. The second part of this paper
112 presents an analysis of the short-period gravity waves observed during 5 NLC seasons,
113 between 2004 and 2008, from the Stockholm University campus (59.4°N). Their
114 characteristics are compared with previous low and mid-latitude and recent high-latitude
115 measurements obtained using airglow data.

117 **2. Observations**

118 NLCs may be seen at mid and high-latitudes due to the scattering of sunlight from a
119 very thin layer of tiny ice particles (~50 nm) which can form and grow in the very cold
120 conditions (~120-140 K) of the high-latitude mesopause region during the summer

months. In this specific latitudinal zone, when the sun lies between 6 and 12° below the horizon (nautical twilight), an observer staying in the darkness will be able to see NLCs which are still in the direct sunlight because to their high altitude. Under these conditions, the sunlight scattering from the atmosphere occurs only at higher altitudes (above at least 40-50 km) and the sky is dark enough to observe NLCs that are seen within the twilight arch as it moves in azimuth with the sun (Fogle and Haurwitz, 1966).

Since summer 2004, pictures of NLCs have been taken from the top floor window of the Arrhenius Laboratory at the university campus in Frescati, Stockholm, Sweden (59.4°N, 18.1°E). A digital camera (Canon PowerShot G5), operating in interval time shooting mode, takes every night hundreds of pictures of the twilight sky at the rate of 1 (2004 and 2005) or 2 (since 2006) pictures per minute, with exposure times varying from 0.5 to 6s, depending on the darkness of the sky. The images are stored on a computer in a digital format. Fig. 1 shows an example of NLCs photographed during the night of 16-17 July, 2005 at 22:30 UT. Many structures with various shapes and sizes are clearly visible in the twilight arch. At the upper edge of the image, above the twilight arch, the NLCs are not visible as they are not illuminated by the sunlight, and in the lower part of the image, below the twilight arch, because the sky is too bright as the sunlight reaches lower atmospheric layers. It is possible to see short-period gravity waves in the center right half of the image, at mid height, but also ripples structures at the same elevation, close to the right edge. Although other structures are present in the image we will restrict our analysis to these two groups of structures. Due to the perspective, it is difficult to determine the parameters of these waves, i.e. their wavelength seems to decrease when they are located further from the observer. The final processed images will permit to make these

measurements using any well-known computational technique, such as a Fast Fourier Transform.

3. Processing technique

Before processing an NLC image, it is necessary to know the observation parameters of the imaging system. The determination of the horizontal and vertical fields of view (FOV_X and FOV_Y) and the azimuth α_{Cam} , elevation β_{Cam} and rotation Rot_{Cam} of the optical axis of the camera is done with a well-proven star calibration method (Garcia et al., 1997). Knowing the exact geographical position of the observer and the exact time of observation, it is possible to identify the stars visible in a “calibration” image acquired when the sky is dark enough, usually at the beginning or at the end of the NLC season. The imager parameters can then be extracted by applying a least-square algorithm as the exact star locations are known.

Due to the observation geometry, the shape of a projected square pixel won't be another square pixel and its size will vary, depending on its elevation and azimuth. Therefore, it is necessary to process each image backward, starting from a pixel of the final image and looking for the corresponding intensity in the original data (Garcia et al., 1997; Pautet and Moreels, 2002).

Subsequently, we need to determine the parameters of the final projected image, starting with its size. It is given by the difference between the ranges corresponding to the highest and lowest visible points of the NLC layer. The elevation β_{Max} of the top of the image, given by

$$\beta_{Max} = \beta_{Cam} + FOV_Y/2 \quad (1)$$

167 Correspond to the closest visible point, located at a distance D_{\min} from the
 168 observation site

$$D_{\min} = (R_E + h_{\text{NLC}}) \cdot \text{asin}(R_{\min} / (R_E + h_{\text{NLC}})) \quad (2)$$

170 Where R_{\min} is defined as

$$R_{\min} = (-R_E \cdot \tan \beta_{\max} + (\tan^2 \beta_{\max} \cdot (R_E + h_{\text{NLC}})^2 + h_{\text{NLC}} \cdot (2 \cdot R_E + h_{\text{NLC}}))^{1/2}) / (1 + \tan^2 \beta_{\max})^2 \quad (3)$$

172 With R_E the average Earth radius, taken equal to 6371 km,

173 and h_{NLC} , the altitude of the NLC layer, taken equal to 82.5 km in this analysis.

174 The elevation β_{\min} corresponding to the furthestmost point has to be chosen depending
 175 on the display itself. In many instances, wave structures are not resolved in the lower part
 176 of the images due to either the increased sky brightness or the decreased resolution, hence,
 177 choosing the bottom image pixel as the furthestmost point is not always relevant.
 178 Choosing a higher minimum elevation also limits the size of the projected image and
 179 improves the resolution of the wave-like structures in the final processed product.

180 The maximum distance D_{\max} is then calculated using the same equation as for D_{\min}

$$D_{\max} = (R_E + h_{\text{NLC}}) \cdot \text{asin}(R_{\max} / (R_E + h_{\text{NLC}})) \quad (4)$$

182 With R_{\max} defined as

$$R_{\max} = (-R_E \cdot \tan \beta_{\min} + (\tan^2 \beta_{\min} \cdot (R_E + h_{\text{NLC}})^2 + h_{\text{NLC}} \cdot (2 \cdot R_E + h_{\text{NLC}}))^{1/2}) / (1 + \tan^2 \beta_{\min})^2 \quad (5)$$

184 The next step is to determine the spatial resolution of the final image in order to fit
 185 the entire projected area. The vertical size (in meters) depends on the distance between
 186 the minimum and the maximum ranges, D_{\min} and D_{\max} , calculated in (2) and (4). The
 187 final value Dist_Y is given by

$$\text{Dist}_Y = 100 \cdot [\text{int}((D_{\max} - D_{\min}) / 100) + 1] \quad (6)$$

Where $\text{int}(x)$ represents the integer part of the number x .

The resolution (in meters per pixel) is obtained by dividing the vertical size of the image Dist_Y by the number of pixels Y_{Img} of the final image

$$\text{Scale} = \text{Dist}_Y / Y_{\text{Img}} \quad (7)$$

The pixel coordinates (X_O, Y_O) of the observation site in the projected image are

$$X_O = X_{\text{Img}} / 2 \quad (8)$$

$$Y_O = ((D_{\text{Max}} - D_{\text{Min}}) / 2 - \text{Scale} \cdot Y_{\text{Img}} / 2) / \text{Scale} + Y_{\text{Img}} \quad (9)$$

Here X_{Img} and Y_{Img} represent the horizontal and vertical pixel sizes of the image, with the origin point $(0, 0)$ corresponding to the top left pixel.

The distance Dist_0 (in meters) between this origin point and the border of the image is given by

$$\text{Dist}_0 = ((D_{\text{Max}} + D_{\text{Min}}) / \text{Scale} - Y_{\text{Img}}) / 2 \quad (10)$$

If we consider a point A in the NLC layer, its coordinates on the projected image will be noted (x_A, y_A) , in the pixels scale and (X_A, Y_A) in the metric scale, with the observation site as the origin. The metric scale coordinates of this point are given by

$$X_A = (x_A - X_{\text{Img}}) / 2 \cdot \text{Scale} \quad (11)$$

$$Y_A = (\text{Dist}_0 + Y_{\text{Img}} - y_A) \cdot \text{Scale} \quad (12)$$

The azimuth angle α_A between the camera axis and the direction of A (see Fig. 2) is

$$\alpha_A = \text{atan}(X_A / Y_A) \quad (13)$$

Garcia et al. (1997) have already calculated the elevation angle β_A of A above the horizon for the similar case of airglow observations. Fig. 3 is a modification of their Fig. 6, adapted to the current situation.

211 The distance r between the projection of the observation site O and the point A at the
 212 NLC altitude is

$$213 \quad r = \sqrt{X_A^2 + Y_A^2} \quad (14)$$

214 The other parameters shown in Fig. 3 are given by

$$215 \quad \varphi = r / (R_E + h_{NLC}) \quad (15)$$

$$216 \quad d = 2(R_E + h_{NLC}) \sin \varphi / 2 \quad (16)$$

$$217 \quad \phi = (\pi - \varphi) / 2 \quad (17)$$

$$218 \quad l = (h_{NLC}^2 + d^2 - 2h_{NLC}d \cos \phi) \quad (18)$$

219 Finally the elevation β_A is equal to

$$220 \quad \beta_A = \cos^{-1} \left(\frac{d \sin \phi}{l} \right) \quad (19)$$

222 For the low elevations, the atmospheric refraction has to be taken into account. In our
 223 case, the Lagrange equation is used for an elevation higher than 13° . The refraction angle
 224 is then given by

$$R = \alpha_0 (1 - \beta_0) \tan \beta_A - \alpha_0 \left(\beta_0 - \frac{\alpha_0}{2} \right) \tan^3 \beta_A \quad (18)$$

225 For normal temperature and pressure conditions

$$226 \quad \alpha_0 = 0.00029255$$

$$227 \quad \beta_0 = 0.001254 \quad \text{then} \quad a = \beta_0 - \alpha_0 / 2 = 0.001108$$

228 At lower elevations, the atmospheric density distribution is more complex and the
 229 refraction angle is approximated by the following equation

$$R = \alpha_0 \left(1 - \frac{\alpha_0}{2} \right) \sqrt{\frac{2}{a}} \sin \beta_A e^{X^2} \left(\frac{\sqrt{\pi}}{2} - \frac{\sqrt{\pi}}{2} \operatorname{erf}(X - \ln \rho_h) \right) \quad (19)$$

230 With the function $\operatorname{erf}(X)$ equal to

$$\text{erf}(x) = \frac{2}{\sqrt{\pi}} \int_0^x e^{-u^2} du = \sum_{k=0}^{\infty} \frac{X^{2k+1}}{k!(2k+1)} \quad (20)$$

231 And

$$232 \quad X = \cos \beta_A / \sqrt{2a} \quad (21)$$

$$\rho_h = e^{-\frac{H_{NLC}}{H_\rho}} \quad (22)$$

$$233 \quad H_\rho = 10400 \text{ m}$$

234 Fig. 4 shows the point A', projection of A on the CCD plane (the original picture). Its
235 coordinates (X_{A'}, Y_{A'}), in meters, are given by

$$Y_{A'} = f \cdot \frac{\cos \beta_{Cam} \tan \beta_A - \sin \beta_{Cam} \cos \alpha_A}{\cos \beta_{Cam} \cos \alpha_A + \sin \beta_{Cam} \tan \alpha_A} \quad (23)$$

$$X_{A'} = f \cdot \tan \alpha_A \cos \beta_{Cam} - f \cdot \frac{\cos \beta_{Cam} \tan \beta_A - \sin \beta_{Cam} \cos \alpha_A}{\cos \beta_{Cam} \cos \alpha_A + \sin \beta_{Cam} \tan \alpha_A} \sin \beta_{Cam} \quad (24)$$

236 Where f is the focal length of the camera lens.

237 Finally, the pixel coordinates (x_{A'}, y_{A'}) of the point A' on the CCD plane are

$$x_{A'} = X_{A'} \cdot X_{Scale} \cdot \cos(-\text{Rot}_{Cam}) + Y_{A'} \cdot Y_{Scale} \cdot \sin(-\text{Rot}_{Cam}) + X_{Img}/2 \quad (25)$$

$$y_{A'} = X_{A'} \cdot X_{Scale} \cdot \sin(-\text{Rot}_{Cam}) - Y_{A'} \cdot Y_{Scale} \cdot \cos(-\text{Rot}_{Cam}) + Y_{Img}/2 \quad (26)$$

238 With X_{Scale} and Y_{Scale} the horizontal and vertical scales, in pixels per meters, of the
239 original image

$$240 \quad X_{Scale} = (X_{Img}/2) / (f \cdot \tan(\text{FOV}_X/2)) \quad (27)$$

$$241 \quad Y_{Scale} = (Y_{Img}/2) / (f \cdot \tan(\text{FOV}_Y/2)) \quad (28)$$

242 It is not necessary to know the focal length of the lens because the coordinates (x_{A'}, y_{A'})
243 will independent of this parameter which disappears when integrating equations (23) to
244 (28) in a computer algorithm.

245 The final results are processed as real numbers, so, for a more accurate measurement
246 of the value of the pixel A, the intensity has to be interpolated using the pixels
247 surrounding the point A' in the original image.

248 The main source of error in the pixel coordinates is due to the uncertainty related to
249 the altitude of the NLC layer. The average value is equal to 82.5 km but it may vary from
250 80 to 85 km (Gadsden and Schröder, 1989). If the altitude difference is ± 2 km, the error
251 on the distance between the observation site and a point of the NLC layer will be $\sim 2\%$.
252 Noctilucent clouds are usually visible when they are located between 100 and 1000 km
253 away from the observer, depending on the latitude of the observation site and the time of
254 the year. For these minimum and maximum ranges, the error on the position of a point of
255 the NLC layer will vary between 2.4 and 13 km (2.4% and 1.3%), respectively.

256 As an example, Fig. 5 shows the projected image of the NLC picture presented in Fig.
257 1, assuming a layer altitude of 82.5 km. The horizontal and vertical fields of view are 53°
258 and 41° , respectively. The NLC layer is presented as seen from the top, with respect to
259 the geographical orientation, and its scale is visible in the bottom right corner. The short-
260 period gravity waves now appear with their real horizontal wavelengths and directions of
261 propagation. Their horizontal observed phase speed may be measured when looking
262 through a sequence of images and the intrinsic horizontal phase speed deduced knowing
263 the velocity and direction of the background wind. Well-developed tools employing
264 Fourier transform techniques were used to measure these parameters (Garcia et al., 1997;
265 Coble et al., 1998). The results for the larger-scale wave (denoted by A) moving
266 northeastward, as indicated by the white arrow, in the right part of the image are:
267 horizontal wavelength $\lambda_h = 29.3 \pm 3$ km, observed horizontal phase speed $v_h = 18.3 \pm 5$ m/s,
268 observed period $\tau = 26.7 \pm 2$ min, and direction of propagation due to North $\theta = 31 \pm 3^\circ$. It

is important to notice that due to the size of the field of view ($53^\circ \times 41^\circ$), the maximum observable wavelength is ~ 100 km, even though longer waves have been reported at the NLC altitude (Carbary et al., 2001; Chandran et al., 2010).

It is also possible to measure the characteristics of the ripple event (noted B), visible on the center right part of the projection: horizontal wavelength $\lambda_h = 5.2 \pm 3$ km, observed horizontal phase speed $v_h = 68.6 \pm 5$ m/s, observed period $\tau = 1.3 \pm 1$ min, and direction of propagation due to North $\theta = 72 \pm 3^\circ$. These values are in the range of previous studies of mesospheric ripple-like waves (e.g., Taylor et al., 1997; Hecht, 2004).

4. Short-period gravity waves analysis

During the past decades, atmospheric gravity waves have been intensely studied using optical instrumentation detecting their signature in the upper atmosphere nighttime airglow emissions (altitudes ~ 80 – 100 km). Most of the observations were conducted from sites located at low (e.g., Taylor et al., 1997; Medeiros et al., 2003; Nakamura et al., 2003; Pautet et al., 2005; Wrasse et al., 2006) or mid-latitudes (e.g., Wu and Killeen, 1996; Hecht et al., 2001; Ejiri et al., 2003). The literature about ground-based short-period gravity wave optical studies at high-latitudes is not very extensive (Clairemidi et al., 1985; Taylor and Henriksen, 1989; Dalin et al., 2004; Nielsen et al., 2006; Nielsen et al., 2009; Bageston et al., 2009) due to the difficult observation conditions like the presence of twilight during the summer months and/or the possible auroral contamination of the faint optical airglow emissions. For these reasons, the data described herein provide a broad and unique dataset to investigate the small-scale gravity waves propagating through the MLT region at a high-latitude site (59.4° N) during the summer months.

Between 2004 and 2008, this imager has run automatically almost every night from May to September, covering the whole local NLC season. If we consider the period extending from the day of the earliest sighting to the day of the latest sighting during these 5 years (May 31-June 1 to August 14-15), the camera has operated during 322 nights. 247 of these nights (77%) were not totally cloudy, allowing seeing possible NLC displays, and during 107 of them (43% of the observable nights) noctilucent clouds were actually visible. From these 107 nights, 32 have been analyzed to determine the characteristics of the gravity wave events appearing in the images. During the other nights, the cloud coverage was too extensive to detect any NLCs or the NLCs were too weak or too far away from the observation site to resolve any wave structure.

After processing the images as described in the first part of this paper, the wave-like patterns were isolated and their parameters (direction of propagation, horizontal wavelength, observed horizontal phase speed and observed period) processed using a well-proven Fast Fourier Transform technique (Garcia et al., 1997; Coble et al., 1998). These wave events were divided in two groups, depending on their aspect and characteristics: the shortest-wavelength, localized and short-lived waves (37 events), often referred as “ripples” or “billows”, and the longer-lived, more spread waves exhibiting longer duration and wavelengths (>10 km) referred as “bands” (30 events). The ripple waves are not described any further in this study because they are mostly due to localized instabilities (e.g., Taylor and Hapgood, 1990; Fritts et al., 1993, 1994; Hecht et al., 1997) and are not thought to provide direct information on freely propagating gravity waves (Hecht, 2004). The second group of events corresponds to the short-period (< 1 h) gravity waves propagating from the troposphere through the MLT region and that

are believed to be responsible for the momentum deposition and part of the global circulation in the upper atmosphere (e.g., Fritts and Alexander, 2003).

The horizontal wavelength λ_x (Fig. 6a), the observed horizontal phase speed v_x (Fig. 6b) and the resulting observed period τ (Fig. 6c) are showed in histogram plots to summarize the characteristics of the 30 short-period gravity wave events observed in the NLC images between 2004 and 2008. The mean values are respectively 25.1 ± 1 km, with 60% of the wavelengths between 20 and 30 km, 27.2 ± 5 m/s with 83% of the phase speeds between 10 and 40 m/s, and 21.9 ± 2 min with 60% of the periods between 10 and 30 min. The comparison with previous long-term studies shows that the average horizontal wavelength is very similar for gravity waves observed in the airglow emissions, at slightly higher altitudes, than in the NC layer. For example, Taylor et al. (1997) (2°S), Nakamura et al. (2003) (7°S) and Medeiros et al. (2003) (23°S), measured values of 24 km, 29 km and 23 km, respectively, for sites located at low latitudes. At mid-latitude locations, the results are similar with horizontal wavelengths reported by Hecht et al. (2001) (40°N) and Ejiri et al. (2003) (44°N) of 25 and 24 km, respectively. In a long-term study at a high-latitude site, conducted during the 2000 and 2001 austral winters from Halley, Antarctica (76°S), Nielsen et al. (2009) obtained an average horizontal wavelength of 26 ± 1 km. During the 2007 austral winter season (April to October 2007), Bageston et al. (2009) observed an horizontal wavelength varying from 10 to 60 km, with a maximum occurrence between 15 and 35 km, at Comandante Ferraz, Antarctica (62°S). All those results are in very good agreement and confirm the systematic global presence of short-period gravity waves at mesospheric altitude. In contrary, the observed horizontal phase speeds obtained from Sweden are different from the previous studies with much smaller values (average 27.2 ± 5 m/s). In the past measurements, the average

phase speeds vary significantly from one site to another, without any apparent relation with the latitude. At low-latitudes, Taylor et al. (1997) (2°S) found a mean value of 48 m/s while Nakamura et al. (2003) (7°S) obtained 56 m/s and Medeiros et al. (2003) (23°S) only 26 m/s. The numbers can also diverge greatly at mid-latitudes; for example Hecht et al. (2001) (40°N) measured an average value of 50 m/s and Ejiri et al. (2003) (44°N) only 35 m/s. The comparison between the Swedish dataset and the measurements made at Halley, Antarctica (76°S), is even more striking with an average value of 48 m/s for the Southern location, almost twice the value obtained in the current study. However, Clairemidi et al. (1985) who operated a near-IR photographic camera at Sodankyla, Finland (67.3°N), reported observed phase speeds of 15.6 m/s varying from 7 to 26 m/s, during a limited 10-day study in Dec 1981-Jan 1982. These results have to be taken carefully because comparison between the datasets would only be possible using the intrinsic horizontal phase speeds, but in most cases, this parameter has not been processed due to a lack of knowledge on the wind velocity at the observation site. Nevertheless, this comparison gives a good estimate of the differences between the studies, especially for similar latitudes and period of the year. The observed periods, which are directly related to the horizontal phase speeds, are also spread over a broad range of values (from 8 to 15 min) and are smaller in the previous studies than for the current measurements (21.9 ± 2 min).

Fig. 7 shows the azimuthal distribution of the observed waves. There exists a strong anisotropy with a majority of the waves propagating towards the north or the north-east (60% of the headings between 330° and 60°). Such asymmetry has been observed before, from both hemispheres, with a preferential poleward motion during the summer months, usually slightly tilted towards the east (e.g., Taylor et al., 1997; Hecht et

al., 2001; Ejiri et al., 2003; Medeiros et al., 2003). Two main reasons have been proposed to explain this anisotropy: Taylor et al. (1993) demonstrated that the background wind can alter the upward flux of waves depending upon their phase speeds and headings. If the wind speed component parallel to the direction of propagation of a wave becomes equal to the observed phase speed of this wave, the wave can be absorbed into the background medium and consequently prohibited in reaching higher altitudes. This so-called critical layer filtering mechanism may explain the strong anisotropy in the wave propagation seen from Stockholm. Localized wind measurements throughout the lower and middle atmosphere are rare and do not exist for the time and location considered here. To address the potential impact of the intervening wind field, we utilize derived winds from an advanced numerical weather prediction system, the Navy Operational Global Atmospheric Prediction System - Advanced Level Physics High-Altitude (NOGAPS-ALPHA) forecast model and data assimilation system, which has recently been extended into the lower MLT region (Hoppel et al., 2009; Eckermann et al., 2009). Localized NOGAPS-ALPHA winds from 69°N has been validated against meteor radar winds (Stevens et al., 2009). In this paper we use winds from 63°N and 18°E, which corresponds to the region north of the observation where majority of the NLCs were observed.

Fig. 8 shows the meridional and zonal background wind components for July 2007 at 0:00 UT. The strong westward zonal wind just below the NLC layer (60 m/s) may justify the small eastward component in the gravity waves propagation but critical layer filtering due to the limited meridional wind (<10 ms below NLC altitude) cannot account for the strong northward heading although it may explain the fact that so many small phase speed events are not filtered out.

Another possible reason, and more likely reason, for the headings anisotropy is the non uniformity in the distribution of the source regions. Atmospheric gravity waves have different origins: orographic forcing by mountains, frontal zones, or tropospheric convection. During the summer months, localized convection develops south of Sweden, mainly over central and western European countries; in addition, the regions further north exhibit weak or no convection. Short-period gravity waves originating from this type of sources, which have been previously observed in the mesospheric airglow over Europe (Taylor and Hapgood, 1988), can be accounted for the anisotropy in the propagation direction. Moreover, Holton et al. (2002) showed that the dominant vertical wavelength of the short-period gravity waves generated by convection depends on the characteristics of the source region. The observed wave phase speeds are also expected to be proportional to the vertical wavelength (through the gravity wave dispersion relationship) and hence to the heating depth. Thus, the limited heating at these latitudes associated with less intense convection compare to observation sites located at lower latitudes, could have excited waves with smaller horizontal phase speeds. In order to make sure that the gravity waves observed from Sweden are generated by close tropospheric convection, it would be necessary to determine the nature of the wave propagation (freely propagating or ducted waves) and associate each wave with a potential source region through a ray-tracing technique.

5. Summary

Noctilucent clouds have been observed and studied for more than 100 years. Their exact composition and the conditions of their formation are still a subject of ongoing research; nevertheless, they are an interesting tool in order to investigate the atmospheric

dynamics, especially the short-period gravity waves propagating through the MLT layer. Standard nighttime airglow measurements are not possible at high-latitude during the summer months because of the persistent twilight and difficult during the winter months due to the auroral contamination. The observation of gravity waves using noctilucent cloud images can be seen as a complementary method for these latitudes.

Since 2004, a camera running automatically every summer night on the Stockholm University campus has obtained a large dataset of NLC pictures, some of them exhibiting gravity wave signatures. The technique described in this paper was developed to process these NLC images in order to easily measure the parameters of the wave events they display. This dataset confirm the presence of short-period gravity waves at high-latitude sites during the summer months and the possibility to successfully study their characteristics, under otherwise difficult conditions. The parameters of 30 wave events have been measured and compared with preceding results obtained using airglow observations, mainly from low or mid-latitude sites. The distribution of the horizontal wavelengths is similar to previous studies but the observed horizontal phase speeds are slower than for the other measurements. This fact cannot be accounted for through critical layer filtering but may instead be a result of weaker source forcing as compared to low- and mid-latitudes. Furthermore, the direction of propagation of the wave events exhibits a strong anisotropy with a majority of the waves heading towards the NNE. This poleward tendency during the summer months has been previously noticed from numerous sites. In the case of the gravity waves observed above Sweden, the distribution of the source regions might be a more preponderant factor than the filtering due to the background wind field. The limited period of observation each year (only the NLC season from June to August) does not allow following the progression of the wave

headings or the observed horizontal phase speeds as a function of the variations in the background wind or the evolution of the gravity wave sources. The source region of the waves is currently under investigation using ray-tracing technique. The results should permit to determine the prevailing nature of the gravity wave motions. Further comparison between current and additional wave measurements and wind data are also needed to confirm the current study and to clarify the role of the gravity waves in the dynamics, the momentum deposition and the global circulation in the upper atmosphere at high-latitudes, and their effects on noctilucent clouds generation and fading. Finally, it would be of great interest to compare the gravity waves observed in NLC images from the ground with the data obtained by satellite-based instruments like CIPS onboard the AIM satellite (Chandran et al., 2009) and with other high-latitude datasets.

Acknowledgements

P.-D. Pautet is grateful to Dr F.T. São Sabbas for inviting him to INPE, through the FAPESP grant 04/12350-7, DEELUMINOS Project, where the collaboration leading to this work was initiated. C.-M. Wrasse would like to thank CNPq for the grant 304277/2008-8.

References

- Bageston, J.V., Wrasse, C.M., Gobbi, D., Takahashi, H., Souza, P.B, 2009. Observation of mesospheric gravity waves at Comandante Ferraz Antarctica Station (62° S). *Ann. Geophys.*, **27**, 2593-2598.
- Carbary, J.F., Morrison, D., and Romick, G.J., 2001. Hemispheric comparison on PMC altitudes, *Geophys. Res. Lett.*, **28**, 725-728.
- Chandran, A., Rusch, D.W., Palo, S.E., Thomas, G.E., Taylor, M.J., 2009. Gravity wave observations in the summertime polar mesosphere from the Cloud Imaging and Particle Size (CIPS) experiment on the AIM spacecraft. *J. Atmos. Solar-Terr. Phys.*, **71**, 3-4, 285-288.
- Chandran, A., Rusch, D.W., Merkel, A.W., Palo, S.E., Thomas, G.E., Taylor, M.J., Bailey, S.M., and Russell III, J.M., 2010. Polar Mesospheric Cloud structures observed from the CIPS experiment on the AIM spacecraft: Atmospheric gravity waves as drivers for longitudinal variability in PMC occurrence, *J. Geophys. Res.*, doi:10.1029/2009JD013185.
- Clairemidi, J., Herse, M., Moreels, G., 1985. Bi-dimensional observation of waves near the mesopause at auroral latitudes. *Planet. Space Sci.*, **33**, 1013-1022.
- Coble, M.R., Papen, G.C., Gardner, C.S., 1998. Computing two-dimensional unambiguous horizontal wavenumber spectra from OH airglow images. *IEEE Trans. Geosci. Remote Sens.*, **36**, 2.
- Dalin, P., Kirkwood, S., Moström, A., Stebel, K., Hoffmann, P., Singer, W., 2004. A case study of gravity waves in noctilucent clouds. *Ann. Geophys.*, **22**, 1875-1884.

Deland, M.T., Shettle, E.P., Thomas, G.E., Olivero, J.J., 2003. Solar backscattered
 ultraviolet (SBUV) observations of polar mesospheric clouds (PMCs) over two solar
 cycles. *J. Geophys. Res.*, **108**, D8, 8445.

Eckermann, S.D., Hoppel, K.W., Coy, L., McCormack, J.P., Siskind, D.E., Nielsen, K.,
 Kochenash, K., Stevens, M.H., Englert, C.R., Hervig, M.E., 2009. High-altitude data
 assimilation system experiments for the northern summer mesosphere season of 2007.
J. Atmos. Terr. Phys., **71** (3-4), 531-551, doi:10.1016/j.jastp.2008.09.036.

Ejiri, M.K., Shiokawa, K., Ogawa, T., Igarashi, K., Nakamura, T., Tsuda, T., 2003.
 Statistical study of short-period gravity waves in OH and OI nightglow images at two
 separated sites. *J. Geophys. Res.*, **108** (D21), 4679.

Fogle, B., Haurwitz, B., 1966. Noctilucent clouds, *Space Science Reviews*, **6**. Gadsden,
 M., 2002. Statistics of the annual counts of nights on which NLCs were seen.
Memoirs Brit. Astron. Assoc., **45**, Aurora Section.

Fritts, D.C., Isler, J.R., Thomas, G.E., Andreassen, Ø., 1993. Wave breaking signatures in
 noctilucent clouds. *Geophys. Res. Lett.*, **20**, 2039.

Fritts, D.C., Isler, J.R., Thomas, G.E., Andreassen, Ø., 1994. Gravity wave breaking in
 two and three dimensions: 2. Three-dimensional evolution and instability structure. *J.*
Geophys. Res., **99**, 8109.

Fritts, D.C., Alexander, M.J., 2003. Gravity wave dynamics and effects in the middle
 atmosphere. *Rev. Geophys.*, **41**(1), 1003, doi:10.1029/2001RG000106.

Gadsden, M., Schröder, W., 1989. *Noctilucent Clouds*, Springer-Verlag, New York.

Gadsden, M., Parviainen, P., 1995. *Observing noctilucent clouds*. International
 Association of Geomagnetism and Aeronomy.

505 Garcia, F.J., Taylor, M.J., Kelley, M.C., 1997. Two-dimensional spectral analysis of
 506 mesospheric airglow image data. *Appl. Optics*, **36**, 29, 7374-7385.

507 Haurwitz, B., 1961. Wave formations in noctilucent clouds. *Planet. Space Sci.*, **5**, 92-98.

508 Hecht, J.H., 2004. Instability layers and airglow imaging. *Rev. Geophys.*, **42**, RG1001,
 509 doi:10.1029/2003RG000131.

510 Hecht, J.H., Walterscheid, R.L., Hickey, M.P., Franke, S.J., 2001. Climatology and
 511 modeling of quasi-monochromatic atmospheric gravity waves observed over Urbana
 512 Illinois. *J. Geophys. Res.*, **106** (D6), 5181–5195.

513 Hines, C.O., 1960. Internal atmospheric gravity waves. *Can. J. Phys.*, **38**, 1441.

514 Holton, J.R., Beres, J.H., Zhou, X.L., 2002 .On the vertical scale of gravity waves excited
 515 by localized thermal forcing. *J. Atmos. Sci.*, **59**(12), 2019.

516 Hoppel, K. W., Baker, N.L., Coy, L., Eckermann, S.D., McCormack, J.P., Nedoluha,
 517 G.E., Siskind, D.E., 2008. Assimilation of stratospheric and mesospheric
 518 temperatures from MLS and SABER into a global NWP model. *Atmos. Chem. Phys.*,
 519 **8**, 6103-6116.

520 Horinouchi, T., Nakamura, T., Kosaka, J., 2002. Convectively generated mesoscale
 521 gravity waves simulated throughout the middle atmosphere. *Geophys. Res. Lett.*,
 522 **29**(21), 2007, doi:10.1029/ 2002GL016069.

523 Jensen, E.J., Thomas, G.E., 1994. Numerical simulations of the effects of gravity waves
 524 on noctilucent clouds. *J. Geophys. Res.*, **99**, D2, 3421-3430.

525 Jesse, O., 1889. Die leuchtenden Nachtwolken. *Meteorol. Zeitung*, **6**, 184–186.

526 Karlsson, B., Kornich, H., Gumbel, J., 2007. Evidence for inter-hemispheric stratosphere-
 527 mesosphere coupling derived from noctilucent cloud properties. *Geophys. Res. Lett.*,
 528 **34**, L16806, doi:10.1029/2007GL030282.

529 Klostermeyer, J., 2002. Noctilucent clouds getting brighter. *J. Geophys. Res.*, **107**, D14,
 530 4195.

531 Leslie, R., 1884. The sky-glows. *Nature*, **30**, 583.

532 Lindzen, R.S., 1981. Turbulence and stress owing to gravity wave and tidal breakdown. *J.*
 533 *Geophys. Res.*, **86**, 9707.

534 Medeiros, A.F., Taylor, M.J., Takahashi, H., Batista, P.P., Gobbi, D., 2003. An
 535 investigation of gravity wave activity in the low-latitude upper mesosphere:
 536 propagation direction and wind filtering. *J. Geophys. Res.*, **108** (D14), 4411.

537 Nakamura, T., Aono, T., Tsuda, T., Admiranto, A.G., Achmad, E., Suranto, 2003.
 538 Mesospheric gravity waves over a tropical convective region observed by OH airglow
 539 imaging in Indonesia. *Geophys. Res. Lett.*, **30** (17), 1882.

540 Nielsen, K., Taylor, M.J., Pautet, P.-D., Fritts, D.C., Mitchell, N., Beldon, C., Williams,
 541 B.P., Singer, W., Schmidlin, F.J., Goldberg, R.A., 2006. Propagation of short-period
 542 gravity wave at high-latitudes during the MaCWAVE winter campaign. *Ann.*
 543 *Geophys.*, **24**, 1227-1243.

544 Nielsen, K., Taylor, M.J., Hibbins, R.E., Jarvis, M.J., 2009. Climatology of short-period
 545 mesospheric gravity waves over Halley, Antarctica (76°S, 27°W). *J. Atmos. Solar-*
 546 *Terr. Phys.*, **71**, 991–1000.

547 Pautet, P.-D., Moreels, G., 2002. Ground-based satellite-type images of the upper-
 548 atmosphere emissive layer. *Appl. Optics*, **41**, 5, 823-831.

549 Pautet, P.-D., Taylor, M.J., Liu, A.Z., Swenson, G.T., 2005. Climatology of short-period
 550 gravity waves observed over northern Australia during the Darwin area wave
 551 experiment (DAWEX) and their dominant source regions. *J. Geophys. Res.*, **110**,
 552 D03S90.

553 Rapp, M., Lübken, F.-J., Müllemann, A., Thomas, G., and Jensen, E., 2002. Small scale
 554 temperature variations in the vicinity of NLC: Experimental and model results, J.
 555 Geophys. Res., 107(D19), 4392, doi:10.1029/2001JD001241.

556 She, C-Y., Lowe, R.P., 1998. Seasonal temperature variations in the mesopause region at
 557 midlatitude: comparison of lidar and hydroxyl rotational temperatures using
 558 WINDII/UARS OH height profiles. J. Atmos. Solar-Terr. Phys., **60** (16), 1573.

559 Stevens, M.H., Siskind, D.E., Eckermann, S.D., Coy, L., McCormack, J.P., Englert, C.R.,
 560 Hoppel, K.W., Nielsen, K., Kochenash, A.J., Hervig, M.E., Randall, C.E., Lumpe, J.,
 561 Bailey, S.M., Rapp, M., Hoffmann, P., Fiedler, J., 2010. Tidally induced variations of
 562 PMC altitudes and ice water content using a data assimilation system, J. Geophys.
 563 Res., under review.

564 Taylor, M.J., Henriksen, K., 1989. Gravity wave studies at polar latitudes.
 565 Electromagnetic Coupling in the Polar Clefts and Caps, P. E. Sandholt and A.
 566 Egeland, Kluwer Academic Publications, Dordrecht, the Netherlands Eds, 421-434.

567 Taylor, M. J., Hapgood, M. A., 1988 .Identification of a thunderstorm as a source of short
 568 period (<1 hr) gravity waves in the upper atmospheric night glow emissions. Planet.
 569 Space Sci., **36**, 975– 985.

570 Taylor, M.J., Hapgood, M.A., 1990. On the origin of ripple-type wave structure in the
 571 OH nightglow emission. Planet. Space Sci., **38**, 1421.

572 Taylor, M.J., Ryan, E.H., Tuan, T.F., Edwards, R., 1993. Evidence of preferential
 573 directions for gravity wave propagation due to wind filtering on the middle
 574 atmosphere. J. Geophys. Res., **98**, 6047.

- 575 Taylor, M.J., Pendleton Jr., W.R., Clark, S., Takahashi, H., Gobbi, D., Goldberg, R.A.,
576 1997. Image measurements of short-period gravity waves at equatorial latitudes. J.
577 Geophys. Res., **102** (D22), 26283–26299.
- 578 Taylor, M.J., Gadsden, M., Lowe, R.P., Zalcik, M.S., Brausch, J., 2002. Mesospheric
579 cloud observations at unusually low latitudes. J. Atmos. Solar-Terr. Phys., **64**, 991–
580 999.
- 581 Wickwar, V.B., Taylor, M.J., Herron, J.P., Martineau, B.A., 2002. Visual and lidar
582 observations of noctilucent clouds above Logan, Utah, at 41.7°N. J. Geophys. Res.,
583 **107**, D7, 4054.
- 584 Witt, G., 1962. Height, structure and displacement of noctilucent clouds. Tellus, **14**, 1-18.
- 585 Wrasse, C.M., Nakamura, T., Takahashi, H., Medeiros, A.F., Taylor, M.J., Gobbi, D.,
586 Denardini, C.M., Fechine, J., Buriti, R.A., Salatun, A., Suranto, Achmad, E.,
587 Admiranto, A.G., 2006. Mesospheric gravity waves observed near equatorial and
588 low–middle latitude stations: wave characteristics and reverse ray tracing results. Ann.
589 Geophys., **24**, 3229-3240.
- 590 Wu, Q., Killeen, T.L., 1996. Seasonal dependence of mesospheric gravity waves
591 (<100km) at Peach Mountain Observatory, Michigan. Geophys. Res. Lett., **23**, 2211–
592 2214.

Figure captions

Fig. 1. Noctilucent cloud image taken from Frescati, Sweden (59.4°N), on July 16th, 2005, at 22:30 UT (0:30 LT).

Fig. 2. Determination of the azimuth angle α_A of a point A of the NLC.

Fig. 3. Plot showing the NLC layer geometry.

Fig. 4. Geometry of the projection of a point of the NLC layer on the CCD plane.

Fig. 5. Projection of the NLC image presented in Fig. 1. Note the short-period gravity wave A on the right part of the image and the ripples B close to the right edge.

Fig. 6: Histogram plots showing the distribution of horizontal wavelengths (a), observed horizontal phase speeds (b) and observed periods (c) of the short-period gravity wave events observed between 2004 and 2008 from Stockholm, Sweden

Fig. 7: Azimuthal plot showing the propagation direction of the waves for the summers 2004 to 2008. Note the anisotropy with the preferential northward heading.

Fig. 8: Plot of the zonal and meridional wind components derived from the NOGAPS-ALPHA assimilation model for July 2007 at 0:00UT and 63°N.

623

624

625

626

627

628



629

Fig. 1. Noctilucent cloud image taken from Frescati, Sweden (59.4°N),

630

on July 16th, 2005, at 22:30 UT (0:30 LT).

631

632

633

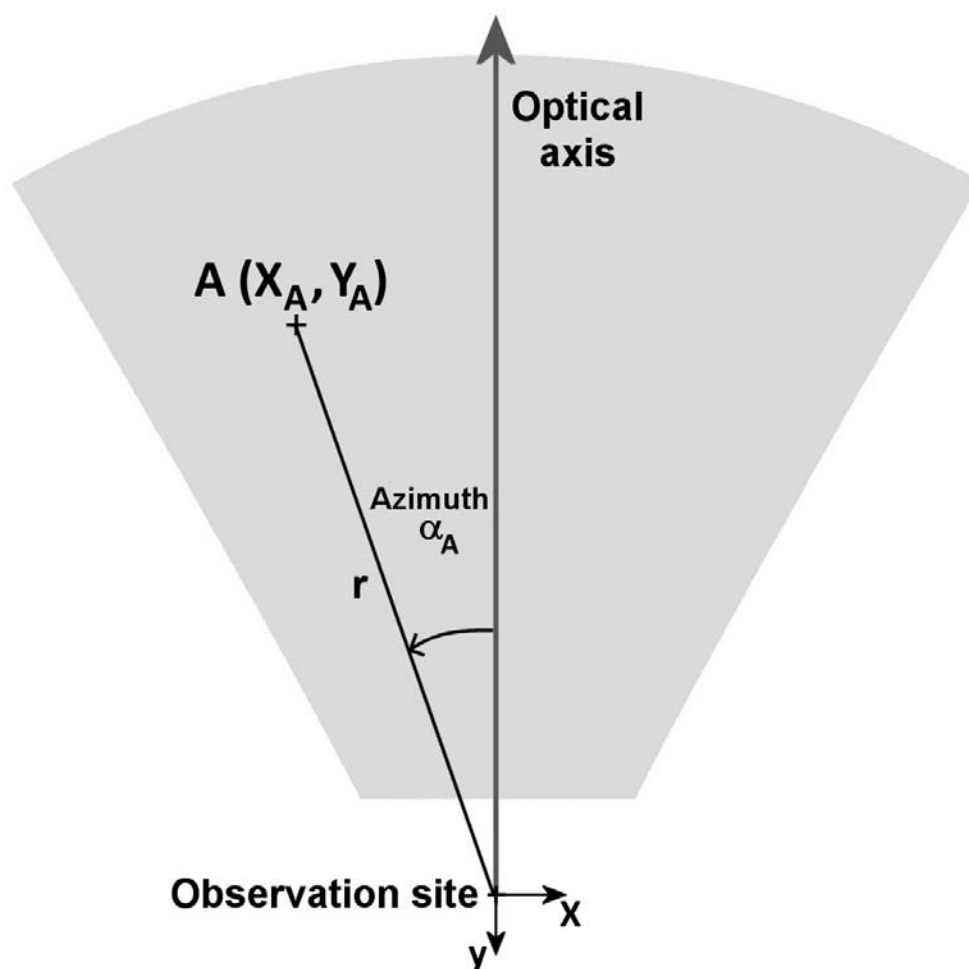
634

635

636

637

638



639

Fig. 2. Determination of the azimuth angle α_A of a point A of the NLC.

640

641

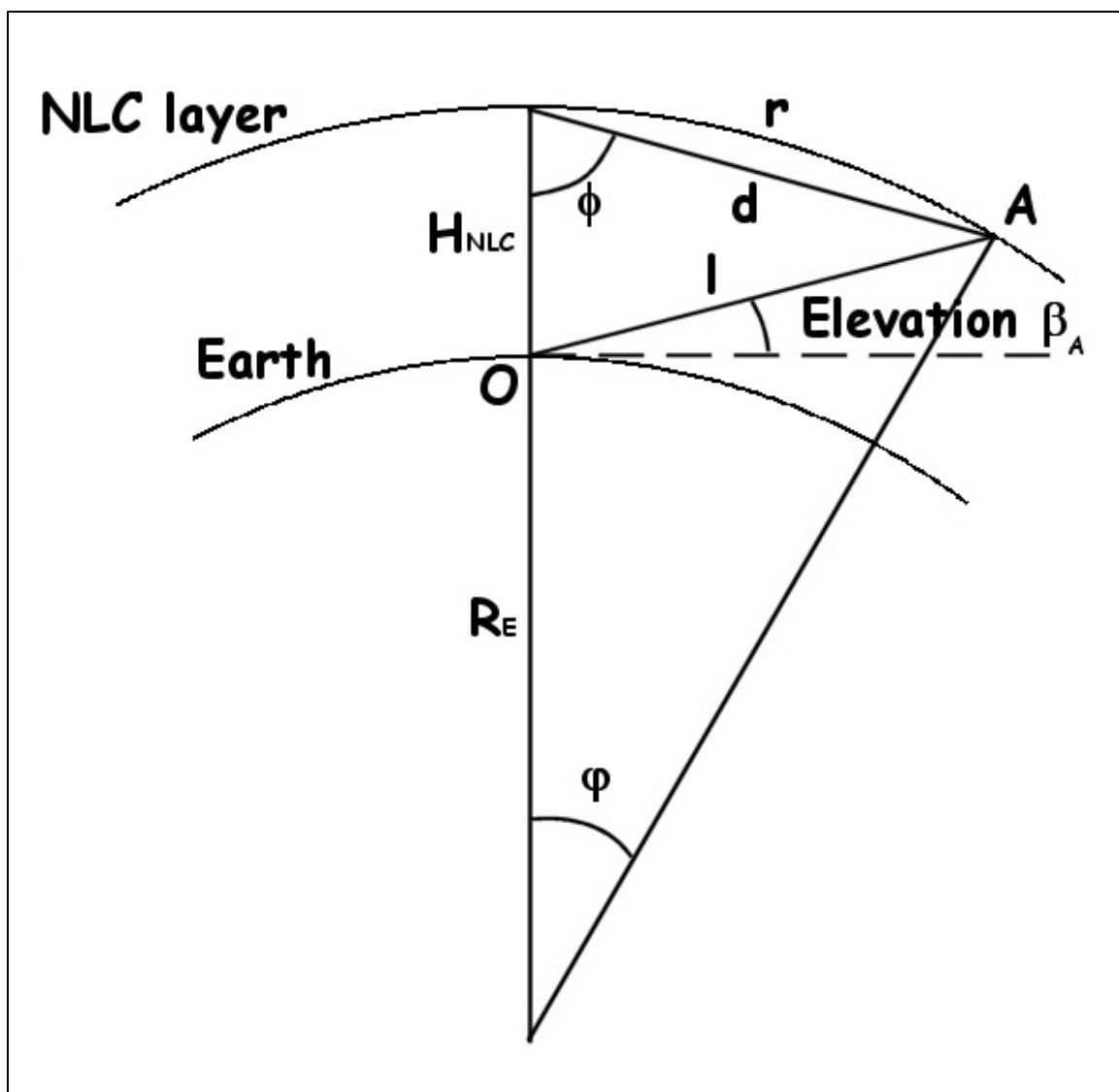
642

643

644

645

646



647

Fig. 3. Plot showing the NLC layer geometry.

648

649

650

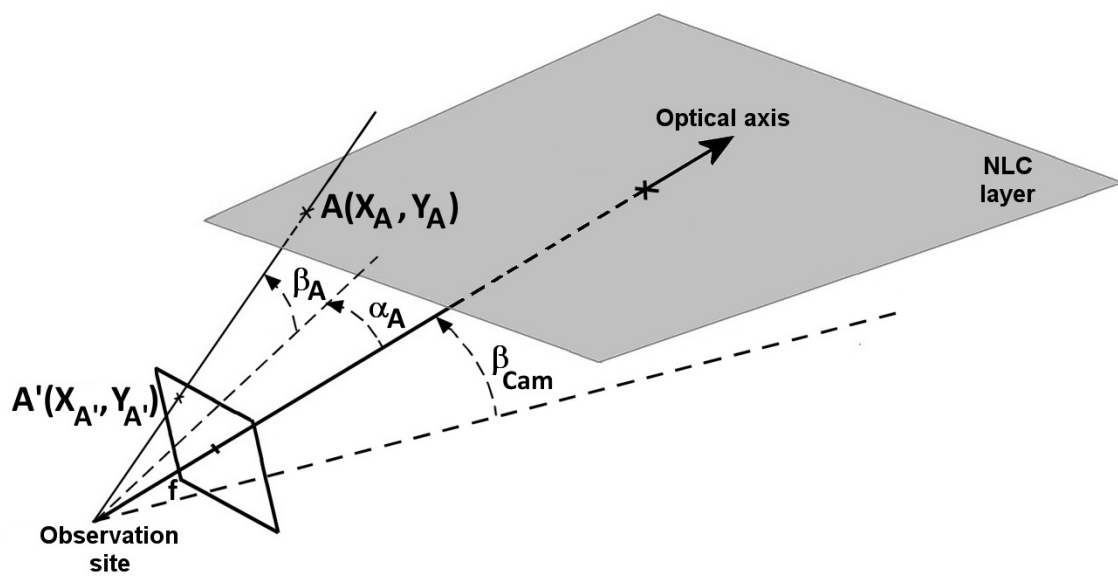


Fig. 4. Geometry of the projection of a point of the NLC layer on the CCD plane.

666

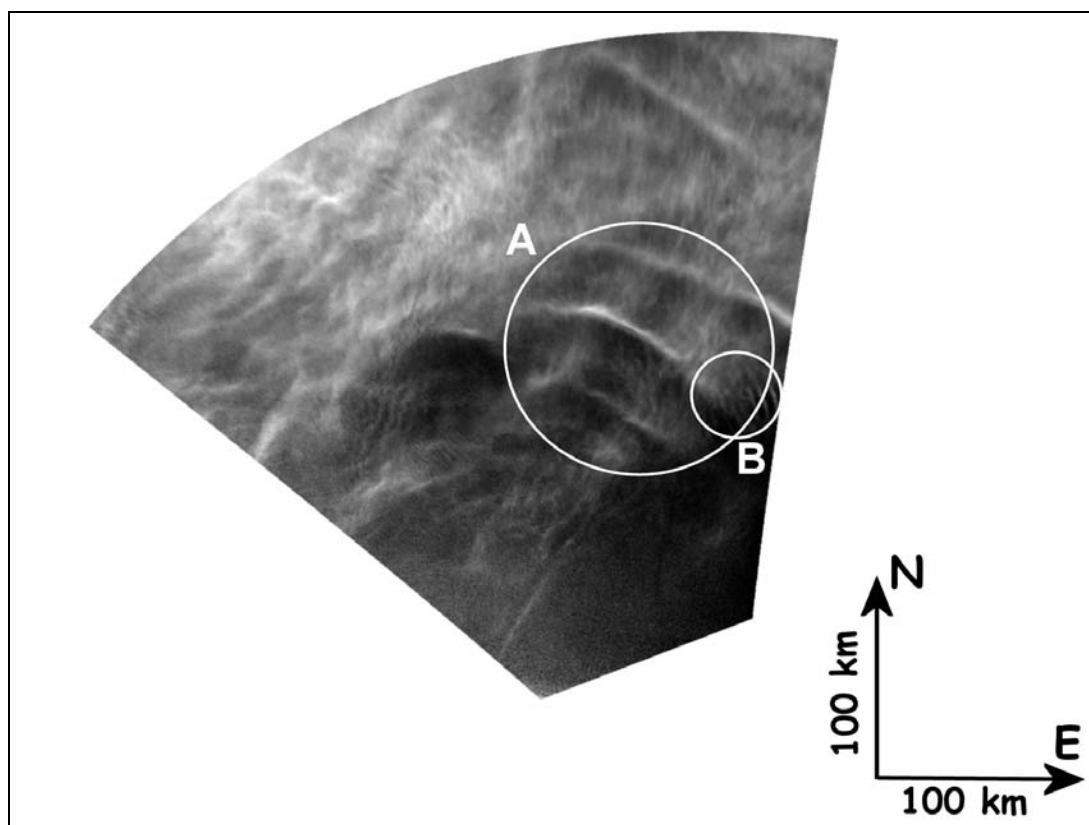
667

668

669

670

671



672

673 Fig. 5. Projection of the NLC image presented in Fig. 1. Note the short-period gravity
674 wave A on the right part of the image and the ripples B close to the right edge.

675

676

677

678

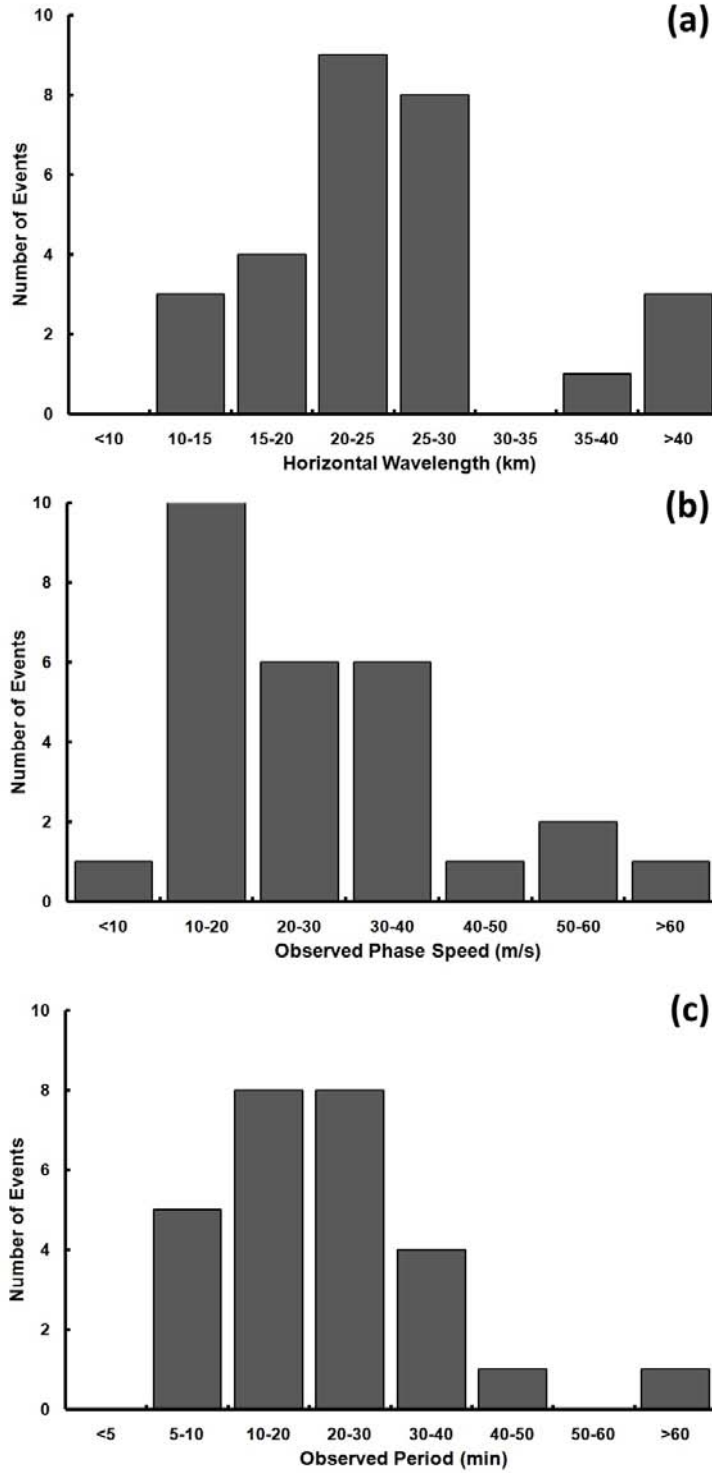


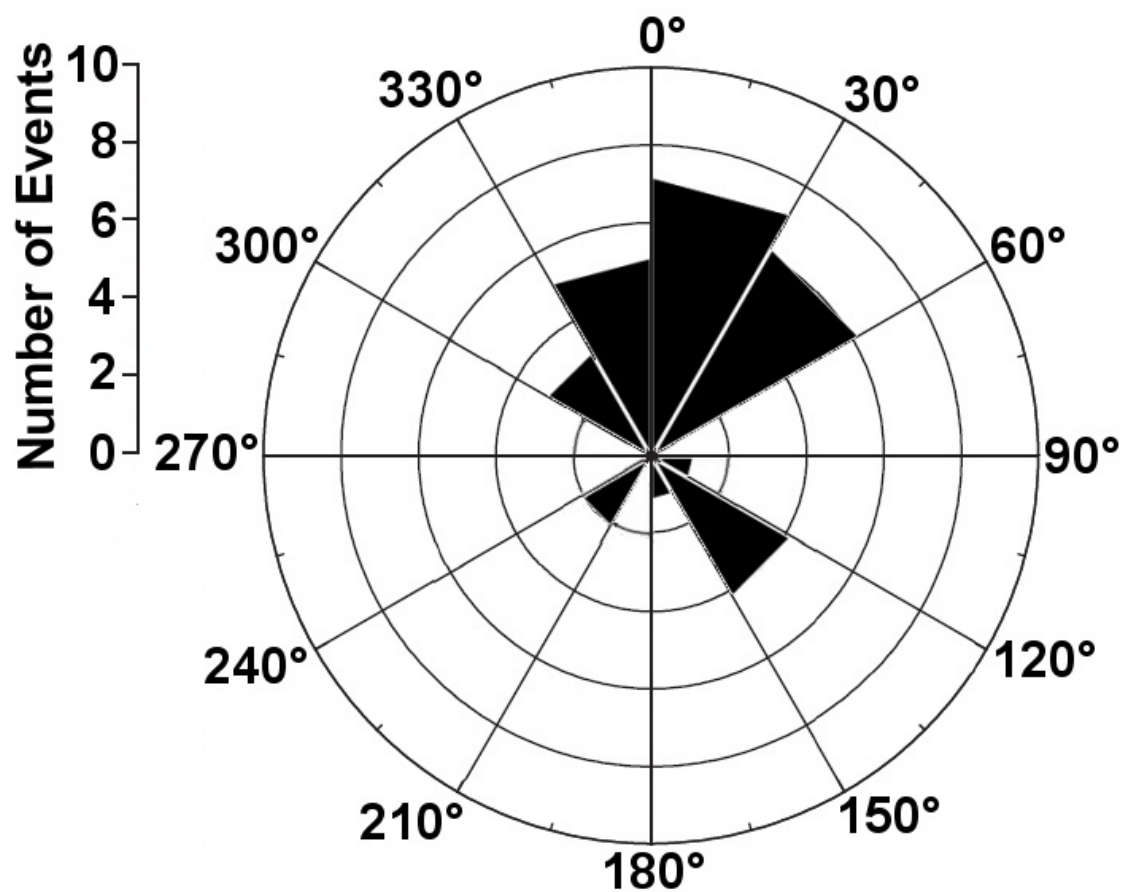
Fig. 6: Histogram plots showing the distribution of horizontal wavelengths (a), observed horizontal phase speeds (b) and observed periods (c) of the short-period gravity wave events observed between 2004 and 2008 from Stockholm, Sweden

703

704

705

706



707 Fig. 7: Azimuthal plot showing the propagation direction of the waves for the summers
708 2004 to 2008. Note the anisotropy with the preferential northward heading.

709

710

711

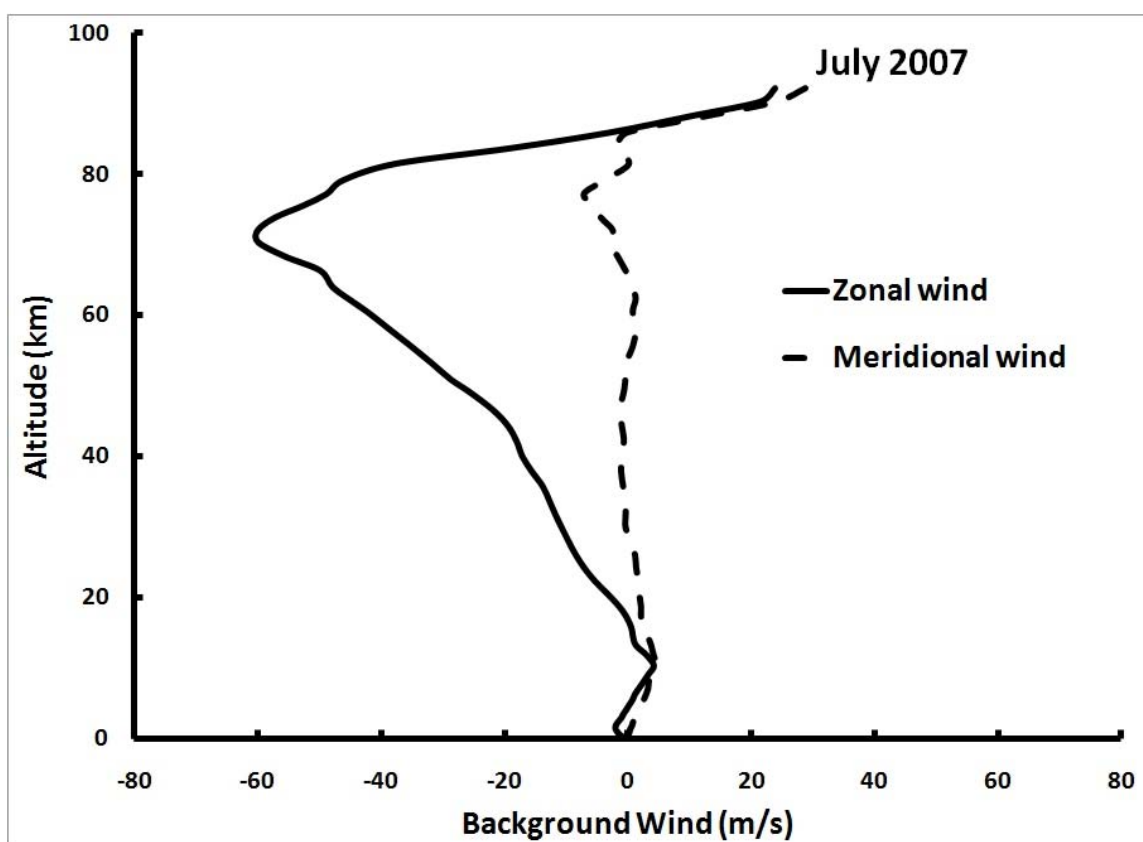
712

713

714

715

716



717 Fig. 8: Plot of the zonal and meridional wind components derived from the NOGAPS-

718 ALPHA assimilation model for July 2007 at 0:00UT and 63°N.

719